Supplementary Material

Manuscript Title: Human retinal pigment epithelium: *in vivo* cell morphometry, multi-spectral autofluorescence, and relationship to cone mosaic

Authors: Granger CE, Yang Q, Song H, Saito K, Nozato K, Latchney LR, Leonard BT, Chung MM, Williams DR, & Rossi EA

Supplementary Methods

Short-wavelength Autofluorescence (SWAF) Optimization Routine

The SWAF optimization routine consisted of first optimizing the deformable mirror (DM) focus. A preset range of approximately 1 D was cycled automatically in 0.1 D steps, usually for 3 cycles. For each, a mechanical shutter opened for 250 ms and the average mean pixel value (MPV) of the five images acquired in that interval was recorded. MPV was then plotted against focus and averaged for all cycles. Focus was then set to be slightly deeper (sclerad) than the SWAF peak for most locations as this empirically resulted in the highest contrast images. Confocal pinhole position was optimized with 250 ms shutter-controlled exposures in a Nelder-Mead[1] optimization routine, as described previously.[2]

Photoreceptor and RPE Cell Analysis

Automatically segmented retinal pigment epithelium (RPE) cell images were subjectively checked and manually corrected by experienced graders by overlaying and comparing the binary and raw images in Photoshop. Corrected segmentations were double-checked by a second grader. Segmented images were analyzed with the MATLAB (The Mathworks Inc., Natick, MA) function *regionprops*. Eccentricity and retinal feature sizes were computed using axial length scaled by the Gullstrand #2 model eye. Segmented cell areas were directly converted from pixels^2 to μm^2 and accounted for the single-pixel wide border separating adjacent cells by dividing the total border area by the number of cells in the ROI and adding the

result to the mean cell area. Similarly, a custom MATLAB program, based on a previously published algorithm,[3] automatically marked the centers of all potential rods and cones in raw photoreceptor ROIs. Binary images with a single pixel at each photoreceptor coordinate were manually corrected and separated into cone and rod images, identifying cones by brighter, larger cell bodies with a dark, contrasted ring and regular spatial pattern, and rods by their smaller diameter and tendency to be clustered. Rod and/or cone ROIs were excluded from photoreceptor analysis in cases of poor image quality where either could not be marked or segregated confidently. For each ROI, a MATLAB script recorded the coordinates and counts of cones and/or rods within each RPE cell, and the RPE cell centroid from binary images. The mean cone-to-RPE-cell ratio and standard deviation were calculated, adjusting the ratio to include cones with coordinates coinciding with RPE cell borders by dividing the number of border cones by the number of RPE cells containing photoreceptors in the ROI, and adding the result to the mean ratio.

The mean participant RPE density and cone-to-RPE ratio were calculated from the weighted mean of data from all participants across eccentricity in bins of 500 μm width, where weights were assigned based on the number of RPE cells within ROIs. Smaller 250 μm bins were used within the central ± 600 μm eccentricity for cone-to-RPE ratio analysis due to the rapidly changing foveal cone density. For each bin, the pooled standard deviation of the contained data was determined by calculating the weighted variance of the data point mean values and the weighted mean of the data point variances, then taking the square root of their sum. Eccentricity error was calculated as the standard deviation of binned ROI eccentricities.

Light Safety

For all combined light sources in SWAF imaging, the maximum exposure duration at any single location was limited to approximately 300 s based on our Rochester Exposure Limit.[4]

Taking overlapping imaging areas into account, we limited exposures to 90 s at each location. For infrared autofluorescence (IRAF) imaging, wavefront sensing at 940 nm was achieved with ≤40 μW at the cornea. Because only infrared light was used in IRAF imaging, thermal damage considerations governed the exposure limit. Following calculations by Schwarz et al.[5] based on the latest ANSI standards,[6] the typical exposure (60 s, 1.5° × 1.5°) from the 796 nm and 940 nm sources was only 3% of the maximum permissible exposure. These low exposures permit repeat imaging at the same location, overlapping imaging, and increased exposure times within the light safety budget for IRAF imaging.

Exposures were also calculated for participants who underwent SWAF and IRAF imaging in the same day, where both thermal and photochemical limits must be considered. Exposure time during imaging is known, but exposure during navigation and optimization prior to imaging must be estimated, where we err towards longer estimates to increase participant safety. The two IRAF exposures delivered at each imaging location are estimated at ~90 s each (30 s optimization, 60 s imaging). In the SWAF system, the measured powers at the cornea were 11.5 μW, 160 μW, and 25 μW for the 532 nm, 796 nm, and 847 nm sources, respectively. The total exposure time at each imaging location was ~45 s for the 532 nm source (15 s optimization, 30 s imaging) and ~75 s for the remaining sources, including navigation, optimization, and imaging. For the smallest imaging field size used (1.2° × 1.2°) the cumulative RREs at each imaging location are 0.42 J/cm^2, 27.7 J/cm^2, 1.61 J/cm^2, and 2.3 J/cm^2 for the 532 nm, 796 nm, 847 nm, and 940 nm sources, respectively. Only the 532 nm source contributes to the photochemical limit, where the calculated RRE is over an order of magnitude below maximum RRE permitted by ANSI at this wavelength (5.8 J/cm^2). Similarly, the cumulative thermal exposure from all sources in this case is only 7% of the ANSI maximum, thus same-day IRAF and SWAF exposures were not at risk for photochemical or thermal damage by ANSI standards.

IRAF Reduction

Masella et al. have shown in both monkeys and humans that there is a reduction in IRAF following exposures of near-infrared (NIR) light[7] below ANSI limits. While IRAF reduction was seen in monkeys even at the lowest tested RRE of 15 J/cm^2, the lowest human exposure tested was ~190 J/cm^2. To determine if IRAF reduction could also be detected in humans at lower exposure levels, we examined two participants (NOR053 and NOR063) who accumulated larger NIR RREs from same-day IRAF and SWAF imaging, using IRAF fundus photos from confocal scanning laser ophthalmoscopy (cSLO) immediately before and after the adaptive optics scanning light ophthalmoscope (AOSLO) imaging session. Only infrared light was used in cSLO imaging, adding a nominal contribution to the total infrared light exposure due to the large imaging field of the clinical instrument. Following methods described by Masella et al.,[7] the IRAF reduction ratio was calculated at two exposed locations and two randomly selected control locations in each participant, where a calculated ratio less than 1 indicates a reduction in IRAF.

Supplementary Discussion

Infrared Autofluorescence (IRAF) Focal Plane

RPE and photoreceptor image quality appeared to decrease quickly when changing focus, even at focal planes approximately 35 μm above and below the subjective best photoreceptor reflectance focus. This observation seems to support our supposition that the system axial resolution is broad enough to provide adequate photoreceptor imaging and RPE AF excitation. As hypothesized in the main text, photoreceptors may also assist in waveguiding the excitation light down to the apical RPE. Greater than 87% of frames were registered with a normalized cross-correlation value >0.75 (mean ~0.88) in each focal plane image sequence, suggesting that defocus blur is the likely cause of image quality reduction rather than registration error.

IRAF Reduction

We have shown IRAF reduction can be detected in humans for NIR exposures similar to the lowest tested in monkeys.[7] These exposures are greater than a typical AO photoreceptor reflectance imaging exposure, but may easily be achieved with other modalities that require long exposures (e.g. non-confocal AO imaging, some AO-OCT methods, and AO assisted visual psychophysics). Additionally, it remains unclear if other wavelengths contribute to IRAF reduction. While no deleterious effects of IRAF reduction have yet been identified,[5,7] there have been no further investigations to determine the mechanism or other potential consequences of the reduction. The reduction in IRAF signal from AO imaging remains a concern for participant safety, especially considering the signal recovery time of many months.[7] Tam et al.[8] reduced exposure time with a larger confocal pinhole in the IRAF detection channel; though this may reduce cell visibility it should still produce IRAF reduction, but to a lesser degree. Future studies should aim to characterize this phenomenon with a better understanding of the IRAF fluorophores and excitation and emission spectra.

AO SWAF as a Clinical Tool

When evaluating high resolution SWAF imaging as a clinical tool for assessing RPE cells, we must consider practical, qualitative and quantitative aspects. A current limitation is the time required for both the collection of large areas using the small AOSLO field of view and manual correction of the segmented cell binary images. Data collection time may be reduced by selecting smaller regions of interest to image; future studies may be guided by our results to focus in on those areas where RPE cells are best imaged. Cell segmentation remains a challenge to overcome, as *in vivo* RPE cell images often have non-discernible cells. Other methods of analysis (e.g. Voronoi domain) rely on a complete mosaic in the analyzed region, which may require assumptions in cell marking that will increase error or inaccuracies.

Advances in automated segmentation and cell analysis, such as may be provided by e.g. machine learning approaches, could greatly improve processing time and the amount of data that may be extracted, as we note in this study only ~15% of the total area imaged in each participant was analyzed, and other useful cell metrics could be applied. Full resolution versions of participant montages (Figs S1-S10) are available online at the Dryad Digital Repository for those who wish to perform further analysis or test analysis software on *in vivo* data; our segmentation images and region of interest (ROI) locations for the cells we segmented are also available upon request to investigators wishing to devise and compare new segmentation algorithms.

Supplementary Tables

Table S1. Scaling and foveal center coordinates used for analysis of SWAF montages provided in this study.

Participant	Foveal Center Pixel Values (x,y)	Scale Factor (μm/pixel)	% of Imaged Area Analyzed in This Study
NOR062	(2176, 2756)	0.863	15.6
NOR064	(4769, 614)	0.872	15.4
NOR053	(6099, 808)	0.870	16.0
NOR065	(5536, 690)	0.878	15.3
NOR057	(4062, 935)	0.859	14.9
NOR063	(5302, 747)	0.841	5.1
NOR047	(5072, 792)	0.854	16.3
NOR073	(4190, 424)	0.814	16.0
NOR011	(5109, 540)	0.923	13.8
NOR025	(4848, 368)	0.897	18.3

Eccentricity in degrees may be calculated for all participants using the scale factor of 333.913 pixels/degree.

Table S2. Comparison of infrared autofluorescence (IRAF) and SWAF segmented RPE cell analysis at the same location.

		IRAF			SWAF		
Partic.	Location	Mean cell density (cells/mm^2)	STD	n	Mean cell density (cells/mm^2)	STD	n
NOR053	Fovea	6631	1690	473	6664	1840	421
NOR053	Temporal	4186	1230	302	4330	1090	264
NOR063	Temporal	5800	1600	307	5608	1640	232

Table S3. IRAF reduction analysis results.

	NOR053 Locations				NOR063 Locations			
	1	2	3	4	1	2	3	4
790 nm RRE (J/cm^2)	27.7	27.7	0	0	20.6	17.1	0	0
IRAF Reduction Ratio	0.87	0.87	1.0	0.98	0.94	0.92	0.99	1.02

Tested locations for each subject are shown in supplementary Figure S15. RRE = retinal radiant exposure.

Supplementary Figures

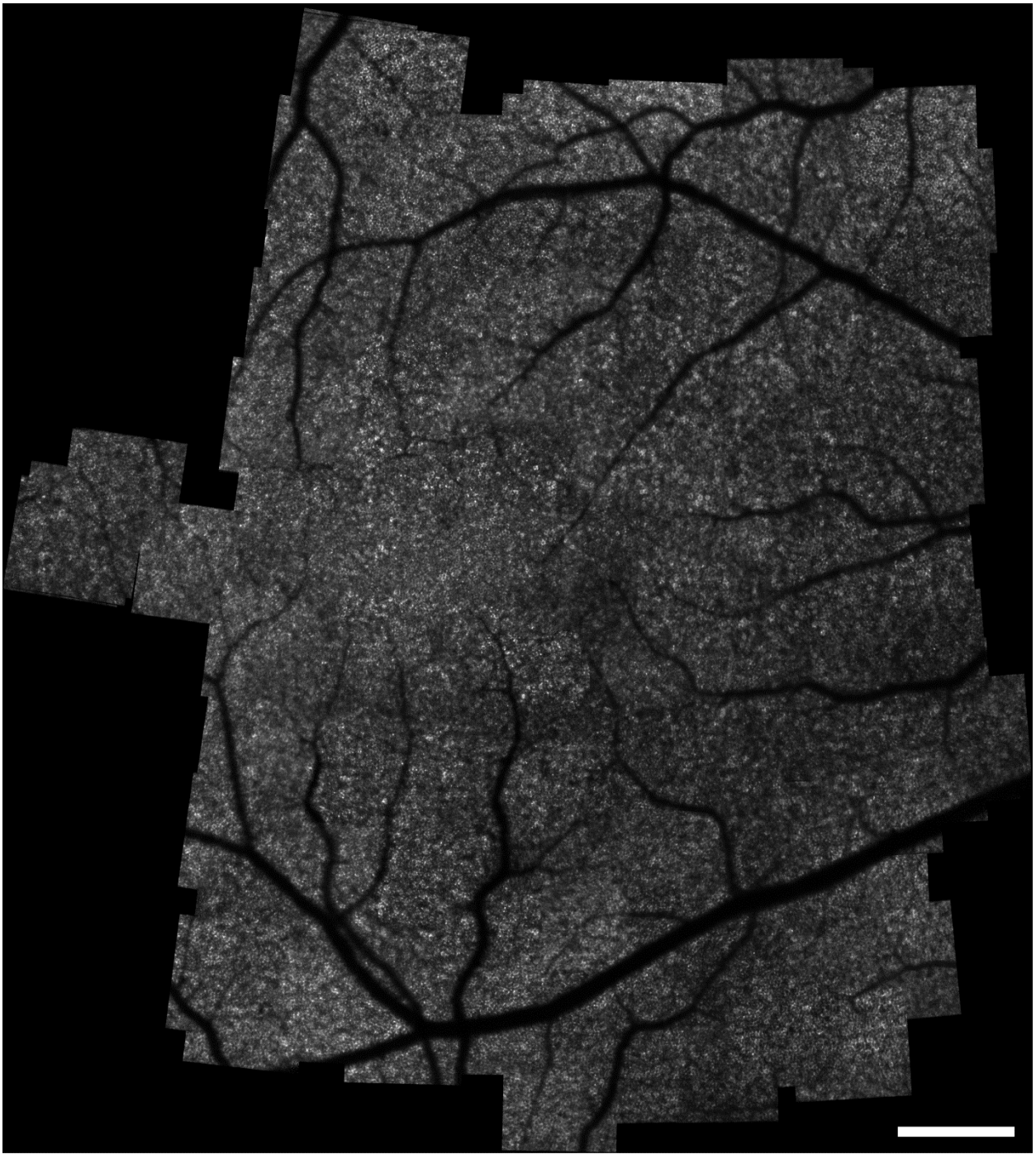

Figure S1. AO SWAF montage from participant NOR062. Scale bar is 500 μm.

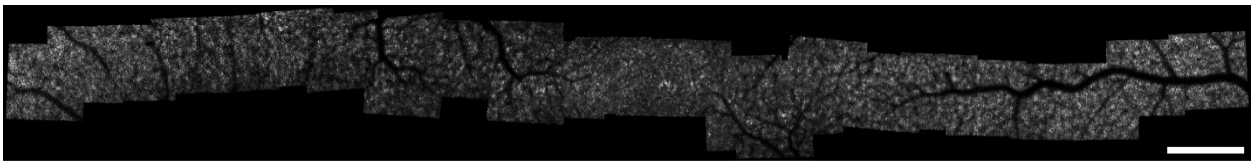

Figure S2. AO SWAF montage from participant NOR064. Scale bar is 500 μm.

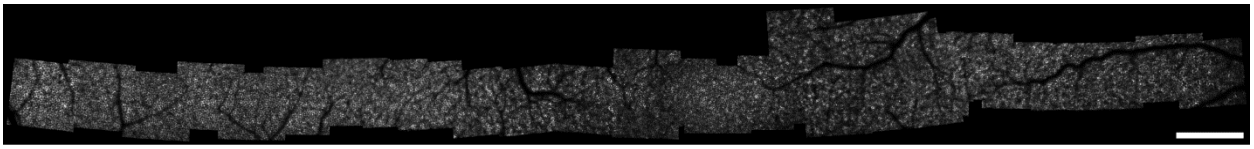

Figure S3. AO SWAF montage from participant NOR053. Scale bar is 500 μm.

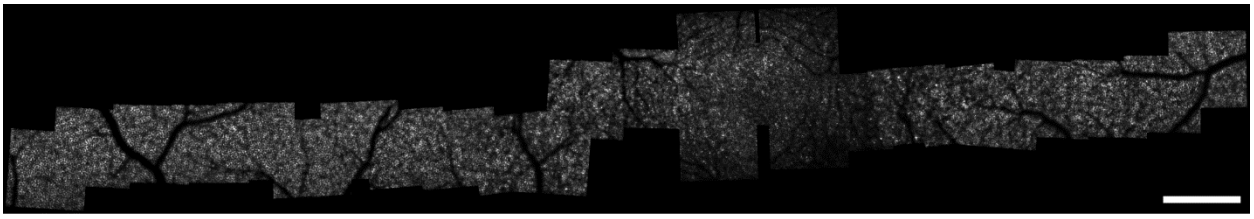

Figure S4. AO SWAF montage from participant NOR065. Scale bar is 500 μm.

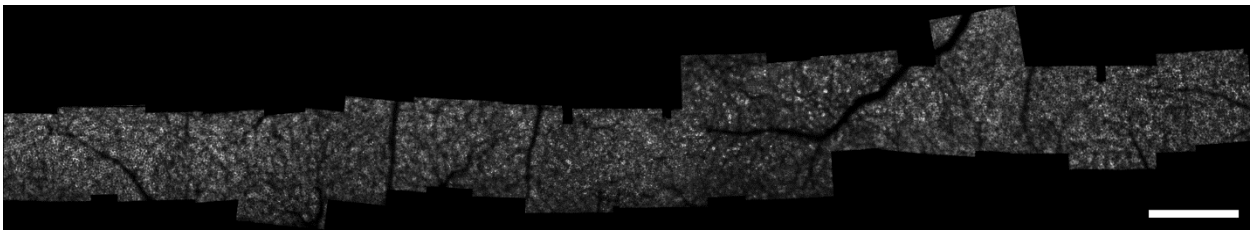

Figure S5. AO SWAF montage from participant NOR057. Scale bar is 500 μm.

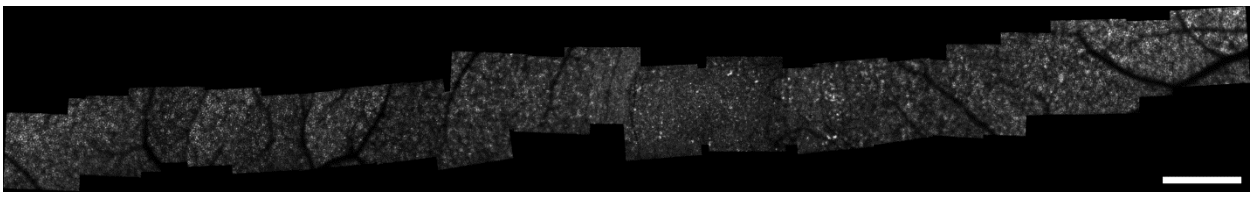

Figure S6. AO SWAF montage from participant NOR063. Scale bar is 500 μm.

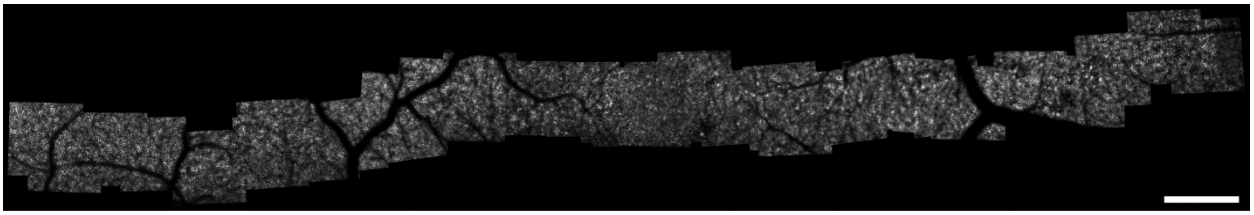

Figure S7. AO SWAF montage from participant NOR047. Scale bar is 500 μm.

Figure S8. AO SWAF montage from participant NOR073. Scale bar is 500 μm.

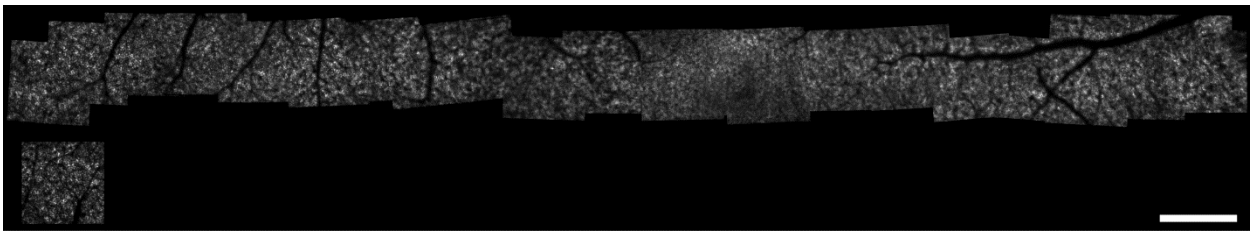

Figure S9. AO SWAF montage from participant NOR011. Scale bar is 500 μm.

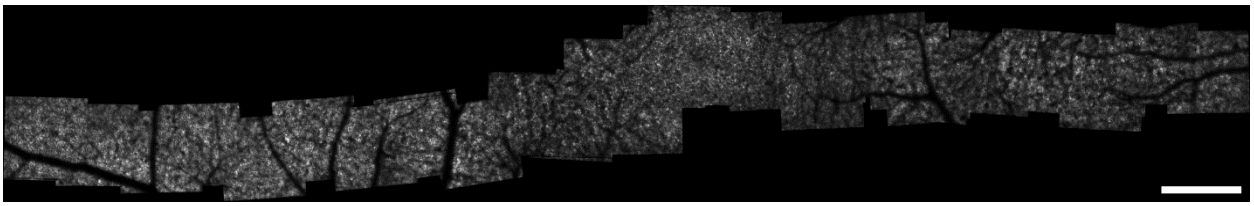

Figure S10. AO SWAF montage from participant NOR025. Scale bar is 500 μm.

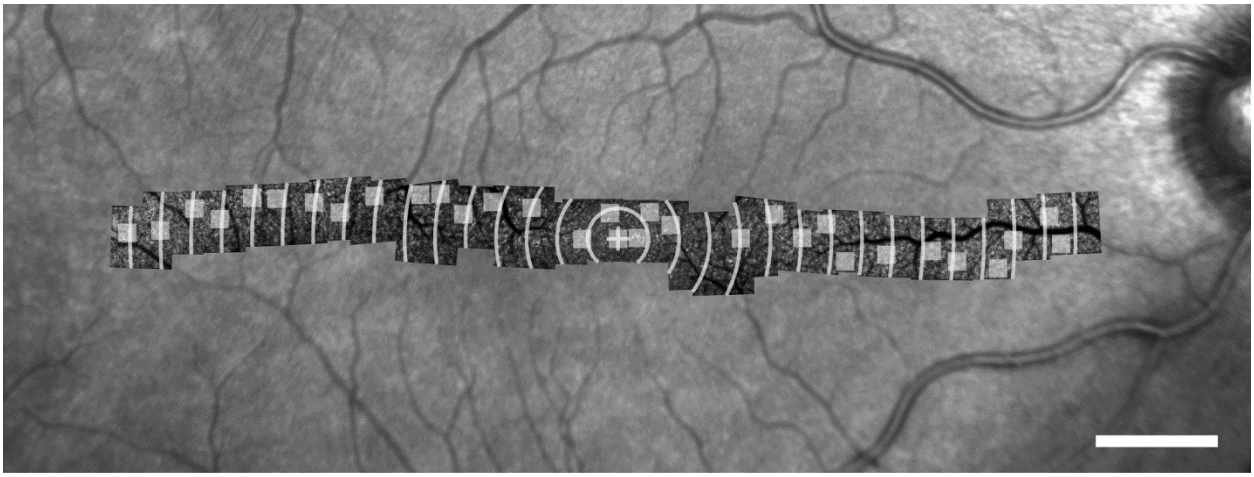

Figure S11. Stitched AO SWAF montage overlaid on a fundus photo for one participant (NOR064), showing the typical imaged area in the SWAF study. Shaded boxes represent 150 µm × 150 µm ROIs used for RPE cell analysis. ROIs were placed at ~250 µm intervals of eccentricity (*concentric rings*) with respect to foveal center (*crosshairs*), avoiding large blood vessel shadows and locations of poor image quality. Scale bar is 1 mm.

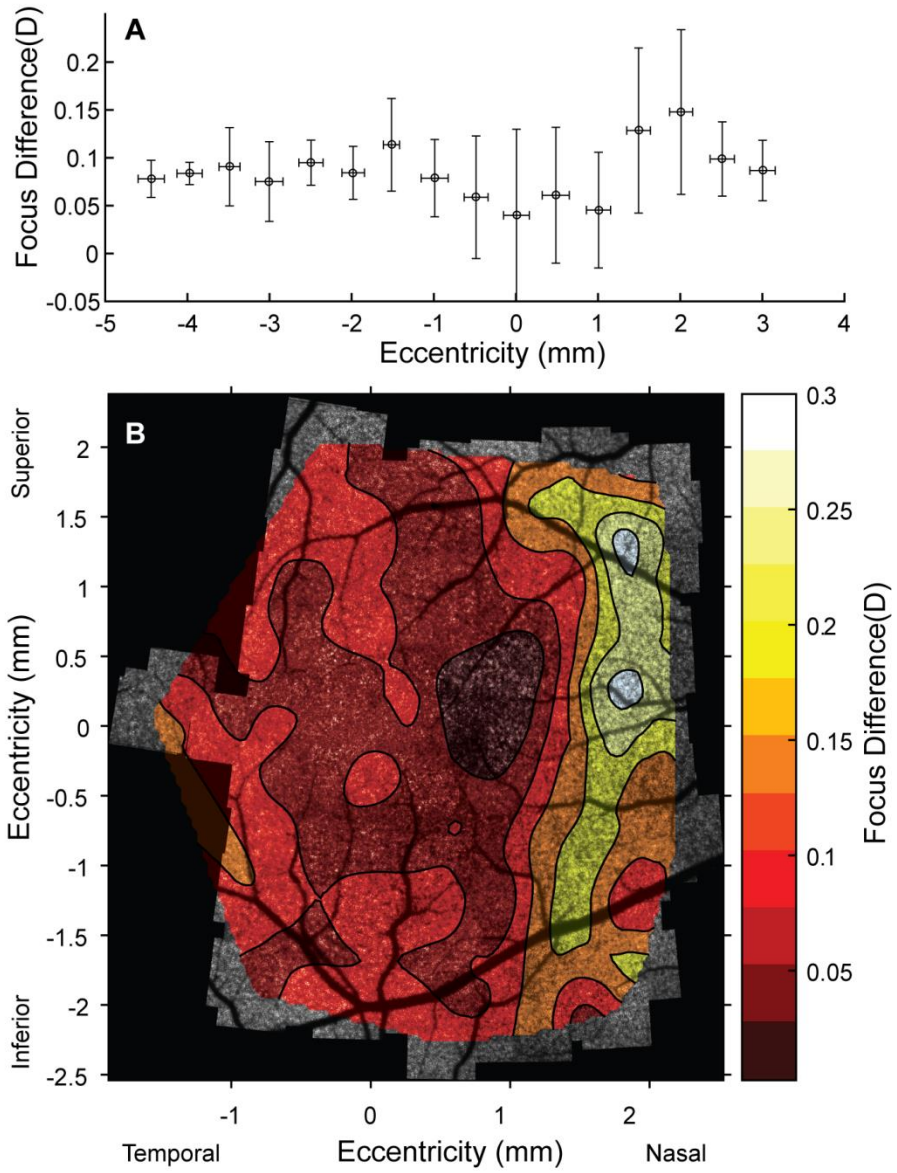

Figure S12. Plots showing difference of best image quality DM focus from peak SWAF focus plotted against eccentricity. (A) Data from 10 participants (331 total images) are binned and averaged (500 μm bin width) across the horizontal meridian, showing a slight decrease and larger variance in the fovea. Error bars are ± 1 standard deviation. (B) A two-dimensional focus difference contour map overlaid on the stitched AO SWAF montage of participant NOR062 shows a pattern similar to (a).

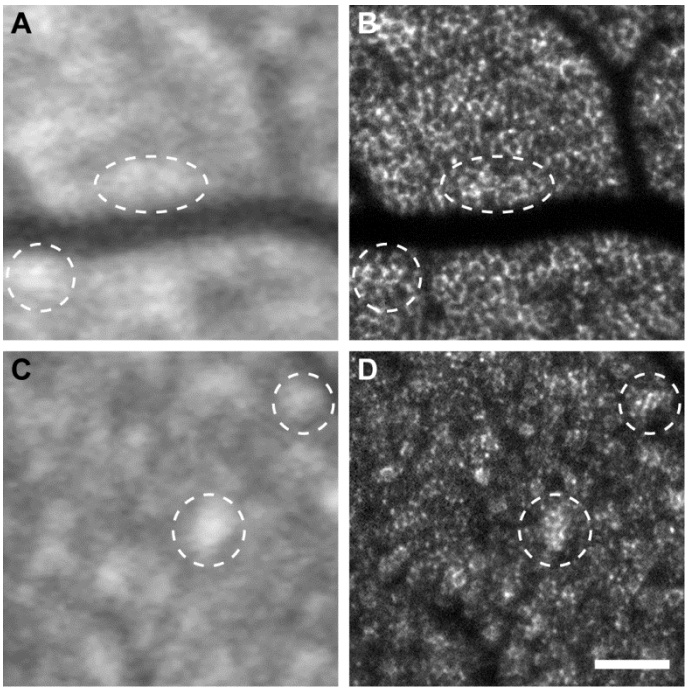

Figure S13. Patches of hyper- AF (*dashed circles*) are often observed in both blue AF cSLO fundus images (A, C) and AO SWAF images (B, D) at the same location. Patches do not appear to be confined to individual cells and sometimes reduce cell contrast. Tissue absorption analysis and AO SWAF and IRAF image comparisons (e.g. Fig. 7) indicate patches are likely from greater signal transmission through gaps in overlying vasculature, however, an abundance of AF material internal or external to cells cannot be ruled out. Examples are from participants NOR064 (A, B) and NOR063 (C, D). Scale bar is 100 μm.

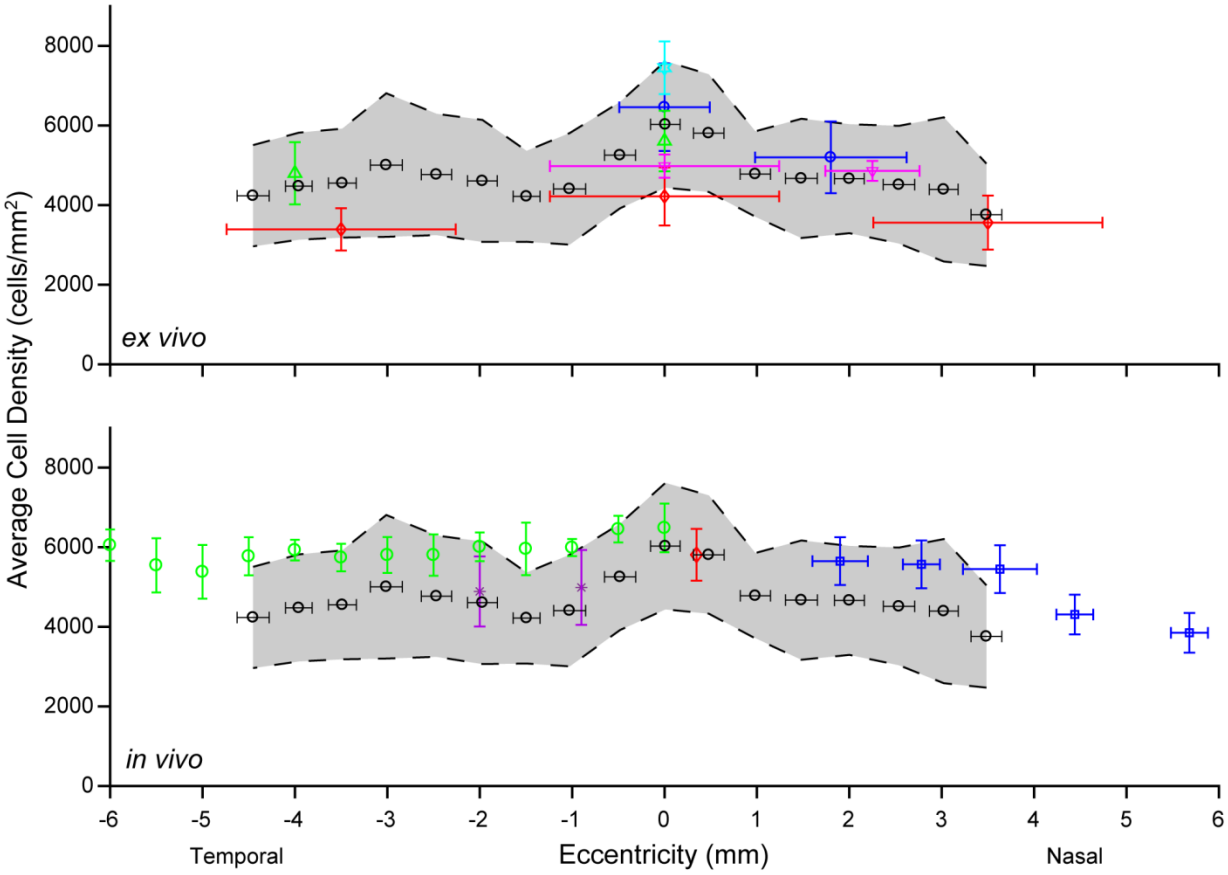

Figure S14. Comparison of RPE cell density measured in this study (*black open circles*) to previous *ex vivo* and *in vivo* measurements. For this study, density data from 10 participants are binned and averaged (500 µm bin width), where the shaded region and horizontal bars represent ± 1 SD. *Ex vivo* data are from Gao and Hollyfield[9] (*cyan star; average of 18 eyes*), Watzke et al.[10] (*green triangles; average of 20 eyes*), Panda-Jonas et al.[11] (*red diamonds; average of 53 eyes*), Del Priore et al.[12] (*magenta triangles; annular average of 22 eyes from 11 participants*), and Ach et al.[13] (*blue circles; annular average of 20 eyes*). In studies where multiple measurements were averaged over a larger area, horizontal error bars represent 68% of the area averaged over. *In vivo* data are from Morgan et al.[14] (*blue squares; binned and averaged data [1 mm bin width] from superior retina in 3 participants*), Tam et al.[15] (*red diamond, averaged data from 3 participants at similar eccentricity of unknown direction*), Liu et al. (2016)[16] (*magenta asterisks; average across 6 participants*), and Liu et al. (2017)[8] (*green*

circles; average across 12 participants). Horizontal error bars in Morgan represent ± 1 SD of binned eccentricity data. Vertical error bars represent ± 1 SD for all.

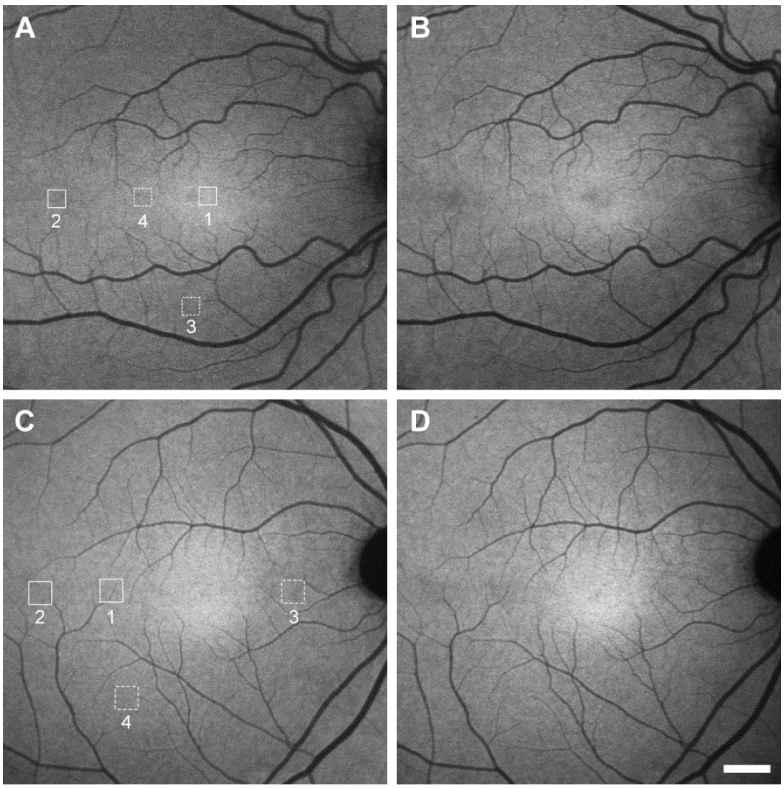

Figure S15. IRAF fundus photographs from participants NOR053 (A, B) and NOR063 (C, D) taken immediately before (A, C) and after (B, D) AO imaging. A reduction in IRAF is observed at exposed locations (*solid boxes*), qualitatively and quantitatively (see Supplementary Table S3). IRAF reduction was not observed at control locations (*dashed boxes*). Scale bar is 1 mm.

References

1. Nelder JA, Mead R. A Simplex Method for Function Minimization. *Comput J*. 1965;7(4):308-313.

2. Rossi EA, Rangel-Fonseca P, Parkins K, et al. In vivo imaging of retinal pigment epithelium cells in age related macular degeneration. *Biomed Opt Express*. 2013;4(11):2527-2539.

3. Li KY, Roorda A. Automated identification of cone photoreceptors in adaptive optics retinal images. *J Opt Soc Am A*. 2007;24(5):1358-1363.

4. Rangel-Fonseca P, Gómez-Vieyra A, Malacara-Hernández D, Wilson MC, Williams DR, Rossi EA. Automated segmentation of retinal pigment epithelium cells in fluorescence adaptive optics images. *J Opt Soc Am A*. 2013;30(12):2595-2604.

5. Schwarz C, Sharma R, Fischer WS, et al. Safety assessment in macaques of light exposures for functional two-photon ophthalmoscopy in humans. *Biomed Opt Express*. 2016;7(12):5148-5169.

6. Laser Institute of America. *ANSI Z136.1 - 2014, American National Standard for Safe Use of Lasers*. Orlando, FL: Laser Institute of America; 2014.

7. Masella BD, Williams DR, Fischer WS, Rossi EA, Hunter JJ. Long-Term Reduction in Infrared Autofluorescence Caused by Infrared Light Below the Maximum Permissible Exposure. *Invest Ophthalmol Vis Sci*. 2014;55(6):3929-3938.

8. Liu T, Jung H, Liu J, Droettboom M, Tam J. Noninvasive near infrared autofluorescence imaging of retinal pigment epithelial cells in the human retina using adaptive optics. *Biomed Opt Express*. 2017;8(10):4348-4360.

9. Gao H, Hollyfield JG. Aging of the human retina. Differential loss of neurons and retinal pigment epithelial cells. *Invest Ophthalmol Vis Sci*. 1992;33(1):1-17.

10. Watzke RC, Soldevilla JD, Trune DR. Morphometric analysis of human retinal pigment epithelium: correlation with age and location. *Curr Eye Res*. 1993;12(2):133-142.

11. Panda-Jonas S, Jonas JB, Jakobczyk-Zmija M. Retinal pigment epithelial cell count, distribution, and correlations in normal human eyes. *Am J Ophthalmol*. 1996;121(2):181-189.

12. Del Priore LV, Kuo Y-H, Tezel TH. Age-Related Changes in Human RPE Cell Density and Apoptosis Proportion In Situ. *Invest Ophthalmol Vis Sci*. 2002;43(10):3312-3318.

13. Ach T, Huisingh C, McGwin J Gerald, et al. Quantitative autofluorescence and cell density maps of the human retinal pigment epithelium. *Invest Ophthalmol Vis Sci*. 2014;55(8):4832-4841.

14. Morgan JIW, Dubra A, Wolfe R, Merigan WH, Williams DR. In vivo autofluorescence imaging of the human and macaque retinal pigment epithelial cell mosaic. *Invest Ophthalmol Vis Sci*. 2009;50(3):1350-1359.

15. Tam J, Liu J, Dubra A, Fariss R. In vivo imaging of the human retinal pigment epithelial mosaic using adaptive optics enhanced indocyanine green ophthalmoscopy. *Invest Ophthalmol Vis Sci*. 2016;57(10):4376-4384.

16. Liu Z, Kocaoglu OP, Miller DT. 3D imaging of retinal pigment epithelial cells in the living human retina. *Invest Ophthalmol Vis Sci*. 2016;57(9):OCT533-OCT543.